REFERENCES

1. S.V. Cherepko and J.C.M. Hwang, VBIC model applicability and extraction procedure for InGaP/GaAs HBT, APMC (2001), 716–721.
2. D. Berger, D. Céll, M. Schröter, M. Malorny, T. Zimmer, and B. Ardouin, HICUM parameter extraction methodology for a single transistor geometry, IEEE BTCM (2002), 116–119.
3. R.B. Nubling, N.H. Sheng, K.C. Wang, M.F. Chang, W.J. Ho, G.J. Sullivan, C.W. Farley, and P.M. Asbeck, 25-GHz HBT frequency dividers, Gallium Arsenide Integrated Circuit (GaAs IC) Symp Dig (1989), 125–128.
4. M. Schröter and T.-Y. Lee, Physics-based minority charge and transit time modeling for bipolar transistors, IEEE Trans Electron Devices 46 (1999), 288–300.

A RANK-REVEALING PRECONDITIONER FOR THE FAST INTEGRAL-EQUATION-BASED CHARACTERIZATION OF ELECTROMAGNETIC CRYSTAL DEVICES

Davy Pissoort,[1] Eric Michielssen,[2] Dries Vande Ginste,[1] and Femke Olyslager[1]
[1] Electromagnetics Group
Department of Information Technology
Ghent University
St.-Pietersnieuwstraat 41, Ghent, Belgium
[2] Radiation Laboratory
Department of Electrical Engineering and Computer Science
University of Michigan
1301 Beal Avenue
Ann Arbor, MI 48109

Received 18 October 2005

ABSTRACT: *A novel rank-revealing shielded-block preconditioner that accelerates the iterative integral-equation-based analysis of wave propagation in electromagnetic crystal (EC) devices is presented. The proposed shielded-block preconditioner exploits the bandgap character of the background electromagnetic crystal in order to achieve both rapid convergence of the iterative solver as well as a low matrix-vector multiplication cost. The versatility and computational efficiency of the shielded-block preconditioner are demonstrated by its application to the analysis of wave propagation in a defectless electromagnetic crystal along an electromagnetic crystal waveguide and out of an electromagnetic crystal horn antenna array.* © 2006 Wiley Periodicals, Inc. Microwave Opt Technol Lett 48: 783–789, 2006; Published online in Wiley InterScience (www.interscience.wiley.com). DOI 10.1002/mop.21475

Key words: *photonic crystals; preconditioning; rank-revealing decomposition*

1. INTRODUCTION

This paper presents a rank-revealing preconditioner that allows the fast integral-equation-based characterization of finite 2D electromagnetic crystal (EC) devices [1]. The ECs studied here comprise periodic constellations of parallel homogeneous dielectric/magnetic circular cylinders residing in a homogeneous background. Infinite and defectless ECs exhibit so-called electromagnetic bandgaps, namely, frequency ranges throughout which no fields are allowed to propagate. EC devices, including (bended) waveguides [2, 3], multiplexers [4–6], super-prisms [7], and horn antennas [8, 9] can be created by removing/adding cylinders from/to finite though otherwise defectless ECs.

In the past, field propagation in finite EC devices often has been analyzed using multiple scattering techniques (MSTs) [10, 11], which solve boundary integral equations in terms of total electric and/or magnetic fields tangential to the EC cylinders' surfaces. Often, these MSTs exploit the cylinders' circular nature by expanding total fields in terms of angular Fourier series of Bessel/Hankel functions. Such MSTs achieve high accuracy with only a few unknowns per cylinder. The principal disadvantage of MSTs is that they require the solution of dense linear systems of equations whose dimensions scale linearly with the number of cylinders, denoted as N_c. The cost of solving these systems directly and iteratively scales as $O(N_c^3)$ and $O(pN_c^2)$, respectively; here, p denotes the number of iterations required. These costs are prohibitive, as EC devices almost invariably are electromagnetically large while containing near-resonant components, thereby leading to large N_c and p and necessitating the use of effectively preconditioned iterative solvers relying on fast matrix-vector multiplication schemes [12].

This paper describes a left shielded-block preconditioner that permits the fast iterative integral-equation-based analysis of field propagation in finite EC devices. Starting from a dense interaction matrix obtained by applying the MST to the analysis of an EC device, the proposed preconditioner is constructed as follows. First, the EC under study is subdivided into a number of physically nonoverlapping blocks of cylinders of roughly equal size. Second, each block of EC cylinders thus obtained is encased in a shield of preset thickness comprising (available) cylinders drawn from neighboring blocks. Third, for each block, the block plus shield self-interaction matrix is inverted and all the rows of the resulting matrix pointing to field variables inside the shield are discarded. Fourth and finally, the shielded-block preconditioner is applied by left-multiplying the original MST global interaction matrix and excitation vector through the collection of all restricted inverses. The inclusion of a shield while forming the preconditioner has two effects. First, it improves the quality of the preconditioner beyond that of a classical (block) diagonal one (which, upon applying the above-outlined procedure, would result in the use of a zero thickness shield), thereby reducing the iteration counts. Second, it (approximately) reduces the interaction rank of different blocks to that intended for proper device operation, thereby allowing nonself group interactions to be accounted for using low-rank matrix-vector product methods. We note that the use of physical-shielding concepts to construct preconditioners that accelerate the convergence of integral-equation solvers pertinent to the analysis of electromagnetic phenomena is not new; ideas similar to those presented here have been used, for example, to accelerate capacitance extraction codes [13]. However, the application of such techniques to the analysis of wave propagation in EC devices yields dramatic improvement over classical preconditioners because they optimally exploit the bandgap character of the underlying EC while maintaining flexibility with regard to the nature of the devices analyzed, that is, without reverting to the use of so-called periodic EC Green functions [14]. The proposed scheme is in contrast to other fast preconditioned integral equation solvers for characterizing EC devices in that it simultaneously addresses preconditioning and acceleration needs.

This paper is organized as follows. Section 2 describes a classical MST for analyzing finite EC devices comprising dielectric/magnetic circular cylinders immersed in a homogeneous background. Section 3 details the construction of the proposed shielded-block preconditioner and demonstrates its effectiveness, both in terms of reducing the iteration counts of MST solvers and accelerating their matrix-vector products. Finally, section 4 elucidates

the application of the proposed scheme to the analysis of an EC horn antenna array.

Note that all sources and fields are assumed time-harmonic with angular frequency ω; temporal dependencies $e^{j\omega t}$ are suppressed. Furthermore, it is assumed that ω lies within the EC bandgap. A z-directed unit vector is denoted as u_z.

2. MULTIPLE SCATTERING TECHNIQUE

This section details an MST for characterizing EC devices comprising N_c as identical, infinite, and z-invariant, homogeneous dielectric/magnetic circular cylinders with radius r, and constitutive parameters (ε_2, μ_2) (permittivity, permeability) that reside in a homogeneous background medium with constitutive parameters (ε_1, μ_1). Let $\boldsymbol{\rho} = (\rho, \phi)$ denote a global transverse position vector in the x–y plane. Likewise, let $\boldsymbol{\rho}_j = (\rho_j, \phi_j)$ denote a local transverse position vector with respect to the center $\boldsymbol{\rho}_j^c$ of cylinder j, $j = 1, \ldots, N_c$. Let $E_z^{\text{inc}}(\boldsymbol{\rho})\boldsymbol{u}_z$ denote a known incident TM$_z$-polarized electric field radiated by impressed sources in the absence of any cylinders. It is assumed that these sources reside outside the cylinders; hence, inside the surface of cylinder i, $i = 1, \ldots, N_c$, $E_z^{\text{inc}}(\boldsymbol{\rho})$ can be expressed as

$$E_z^{\text{inc}}(\boldsymbol{\rho}) = -\frac{\omega\mu_1}{4}\sum_{n=-\infty}^{+\infty} C_n^i J_n(k_1\rho_i)e^{jn\phi_i}, \quad \text{for } \rho_i \le r, \tag{1}$$

with known C_n^i. In the presence of the cylinders, the total field $E_z^{\text{tot}}(\boldsymbol{\rho})\boldsymbol{u}_z$ is observed. The difference between the total and incident fields is the scattered field $E_z^{\text{sca}}(\boldsymbol{\rho})\boldsymbol{u}_z$, namely, $E_z^{\text{tot}}(\boldsymbol{\rho}) = E_z^{\text{inc}}(\boldsymbol{\rho}) + E_z^{\text{sca}}(\boldsymbol{\rho})$. In what follows, the scattered field is decomposed as $E_z^{\text{sca}}(\boldsymbol{\rho}) = \sum_{j=1}^{N_c} E_z^{\text{sca},j}(\boldsymbol{\rho})$, with $E_z^{\text{sca},j}(\boldsymbol{\rho})$ representing the z-component of the electric field scattered by cylinder j; this field can be expressed in local coordinate systems centered about cylinders j and $i \neq j$ as

$$E_z^{\text{sca},j}(\boldsymbol{\rho}) = -\frac{\omega\mu_1}{4}\sum_{n=-\infty}^{+\infty} A_n^j H_n^{(2)}(k_1\rho_j)e^{jn\phi_j}, \quad \text{for } \rho_j > r \tag{2}$$

$$= -\frac{\omega\mu_1}{4}\sum_{n=-\infty}^{+\infty} A_n^j \sum_{m=-\infty}^{+\infty} H_{m-n}^{(2)}(k_1R_{ij}) \times e^{j(n-m)\Phi_{ij}} J_m(k_1\rho_i)e^{jm\phi_i}, \quad \text{for } \rho_i < R_{ij} - r. \tag{3}$$

Likewise, the total electric field inside the j^{th} cylinder can be expressed as follows:

$$E_z^{\text{tot}}(\boldsymbol{\rho}) = -\frac{\omega\mu_2}{4}\sum_{n=-\infty}^{+\infty} B_n^j J_n(k_2\rho_j)e^{jn\phi_j}, \quad \text{for } \rho_j < r. \tag{4}$$

In the above equations, A_n^j and B_n^j are unknown coefficients describing the scattered and total fields outside and inside cylinder j. $k_\alpha = \omega\sqrt{\varepsilon_\alpha\mu_\alpha}$ ($\alpha = 1, 2$) is the wavenumber of the unbounded medium with constitutive parameters (ε_α, μ_α), and $J_n(\cdot)$ and $H_n^{(2)}(\cdot)$ are the n^{th}-order first-kind Bessel and second-kind Hankel functions, respectively. Expression (3) follows from (2) through application of the Hankel function addition theorem ([15], p. 232, Eqs. (5)–(103); also, in (3) $R_{ij} = |\boldsymbol{\rho}_{ij}^c|$ and $\Phi_{ij} = \arctan[(\boldsymbol{\rho}_{ij}^c \cdot \boldsymbol{u}_y)/(\boldsymbol{\rho}_{ij}^c \cdot \boldsymbol{u}_x)]$ are the length and the angle with regard to the positive x-axis of the vector $\boldsymbol{\rho}_{ij}^c = \boldsymbol{\rho}_j^c - \boldsymbol{\rho}_i^c$ connecting the centers of cylinders i and j. Because the cylinder radius r is small compared to the wavelength and because the cylinders are assumed sufficiently separated from one another as well as from the impressed sources, the range of the modal index n always can be restricted to $n = -K, \ldots, K$, with K a small positive integer.

Components of total electric and magnetic fields tangential to surface S_i, $i = 1, \ldots, N_c$, are continuous across S_i. By expressing the magnetic field tangential to the EC cylinder surfaces in terms of the normal derivative to the surface of the z-directed electric field, these continuity conditions can be expressed as

$$E_z^{\text{inc}}(\boldsymbol{\rho})|_{\boldsymbol{\rho}\in S_i^+} + \sum_{j=1}^{N_c} E_z^{\text{sca},j}(\boldsymbol{\rho})|_{\boldsymbol{\rho}\in S_i^+} = E_z^{\text{tot}}(\boldsymbol{\rho})|_{\boldsymbol{\rho}\in S_i^-}, \tag{5}$$

$$\frac{1}{\mu_1}\frac{\partial E_z^{\text{inc}}(\boldsymbol{\rho})}{\partial\rho_i}\bigg|_{\boldsymbol{\rho}\in S_i^+} + \frac{1}{\mu_1}\sum_{j=1}^{N_c}\frac{\partial E_z^{\text{sca},j}(\boldsymbol{\rho})}{\partial\rho_i}\bigg|_{\boldsymbol{\rho}\in S_i^+} = \frac{1}{\mu_2}\frac{\partial E_z^{\text{tot}}(\boldsymbol{\rho})}{\partial\rho_i}\bigg|_{\boldsymbol{\rho}\in S_i^-}. \tag{6}$$

Here, S_i^+ and S_i^- denote surfaces residing just outside and inside S_i, respectively. Insertion of (1)–(4) into (5)–(6) and testing of the resulting equations with a set of harmonic functions $e^{jn\phi_i}$, $n = -K, \ldots, K$, leads to a linear set of $2(2K+1)N_c$ equations in terms of A_n^j and B_n^j, $n = -K, \ldots, K$; $j = 1, \ldots, N_c$:

$$\mu_1 C_n^i J_n(k_1r) + \mu_1 A_n^i H_n^{(2)}(k_1r) + \mu_1 \sum_{j\neq i}\sum_m A_m^j H_n^{(2)}(k_1R_{ij}) \times e^{j(m-n)\Phi_{ij}} J_n(k_1r) = \mu_2 B_n^i J_n(k_2r), \tag{7}$$

$$k_1 C_n^i J_n'(k_1r) + k_1 A_n^i H_n^{(2)'}(k_1r) + k_1 \sum_{j\neq i}\sum_m A_m^j H_n^{(2)}(k_1R_{ij}) \times e^{j(m-n)\Phi_{ij}} J_n'(k_1r) = k_2 B_n^i J_n'(k_2r). \tag{8}$$

While these equations could be solved for the A_n^j and B_n^j by brute force, their inspection reveals that (interior) unknowns B_n^j can be eliminated in favor of (exterior) unknowns A_n^j (on a cylinder by cylinder basis), leaving only $(2K+1)N_c$ linear equations:

$$\frac{k_2\mu_1 H_n^{(2)}(k_1r)J_n'(k_2r) - k_1\mu_2 H_n^{(2)'}(k_1r)J_n(k_2r)}{k_2\mu_1 J_n^2(k_1r)J_n'(k_2r) - k_1\mu_2 J_n'(k_1r)J_n(k_2r)} A_n^i + \sum_{j\neq i}\sum_m H_n^{(2)} \times (k_1R_{ij}) \times e^{j(m-n)\Phi_{ij}} A_m^j = -C_n^i, \tag{9}$$

or, in matrix notation, $\boldsymbol{ZA} = \boldsymbol{C}$.

3. SHIELDED-BLOCK PRECONDITIONER

This section details the proposed rank-revealing shielded-block preconditioner. Instead of solving (9) directly, an equivalent system of equations,

$$\boldsymbol{MZA} = \boldsymbol{MC}, \tag{10}$$

where the preconditioner $\boldsymbol{M}$ approximates $\boldsymbol{Z}^{-1}$, is constructed and solved iteratively. In what follows, $\tilde{\boldsymbol{Z}}$ denotes the preconditioned interaction matrix $\boldsymbol{MZ}$.

3.1. Construction of the Shielded-Block Preconditioner

The proposed shielded-block preconditioner can be seen as an improvement on a classical block-diagonal preconditioner. To construct the latter, the EC device first is subdivided into N_g contiguous blocks of cylinders. Next, for each block j, the submatrix $\boldsymbol{Z}_j$ of $\boldsymbol{Z}$ describing all of its cylinders' self- and mutual-interactions is inverted. Finally, all resulting inverses are collected into a block-diagonal matrix to form an approximate inverse $\boldsymbol{M}$ of

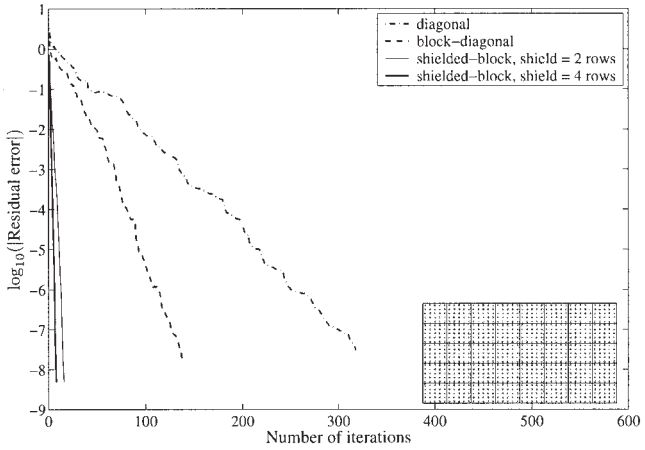

Figure 1 Residual error vs. iteration number for a rectangular defectless EC

$\boldsymbol{Z}$. The construction of the shielded-block preconditioner proceeds only slightly differently. First, for each block the submatrix $\hat{\boldsymbol{Z}}_j$ describing self- and mutual-interactions of its cylinders plus those residing in a shield around it, namely, a physical jacket of preset thickness that surrounds the block and comprises cylinders present in the block's immediate environment, is inverted. Next, from $\hat{\boldsymbol{Z}}_j^{-1}$, only the rectangular submatrix $\boldsymbol{Y}_j$ comprising rows pointing to variables inside block j are retained. Finally, all $\boldsymbol{Y}_j$ are arranged into a new approximate inverse $\boldsymbol{M}$ of $\boldsymbol{Z}$; this new $\boldsymbol{M}$ is no longer block-diagonal as its block constituents overlap along the column index.

3.2. Effect on Preconditioning and Iteration Counts

This section compares the performance of the shielded-block preconditioner to that of diagonal and block-diagonal preconditioners via their application to two simple EC devices, namely, a defectless EC and an EC waveguide formed by removing one row of cylinders from a defectless EC. The defectless EC is composed of dielectric cylinders with constitutive parameters $(\varepsilon_2, \mu_2) = (11.56\varepsilon_0, \mu_0)$ and radius $r = 0.18a$, that are spaced by a from center to center along the x and y directions—a is called the lattice constant—and that are residing in free space, namely, $(\varepsilon_1, \mu_1) = (\varepsilon_0, \mu_0)$. Both structures comprise 40 rows of 25 cylinders, that is, a total of $N_c = 1000$ cylinders, which with $K = 1$ translates into 3000 unknowns. For illustrative purposes, the block-diagonal and shielded-block preconditioners are constructed by subdividing the EC devices into blocks of 5×5 cylinders. Figures 1 and 2 show the evolution of the residual error versus the iteration count for these EC devices when solving (10) with the quasi-minimal residual (QMR) routine [16] and this for the three different types of preconditioners. Both structures are excited by a z-directed unit-strength electric-line current. For the defectless EC, this line current is located outside the crystal; for the EC waveguide, it is located inside the EC waveguide's channel. When using only a diagonal preconditioner, the residual error quasi-stagnates during many iterations for the EC waveguide. The block-diagonal and shielded-block preconditioners entirely alleviate this phenomenon. Moreover, for both EC configurations studied, application of the shielded-block preconditioner leads to a smaller iteration count than the block-diagonal preconditioner.

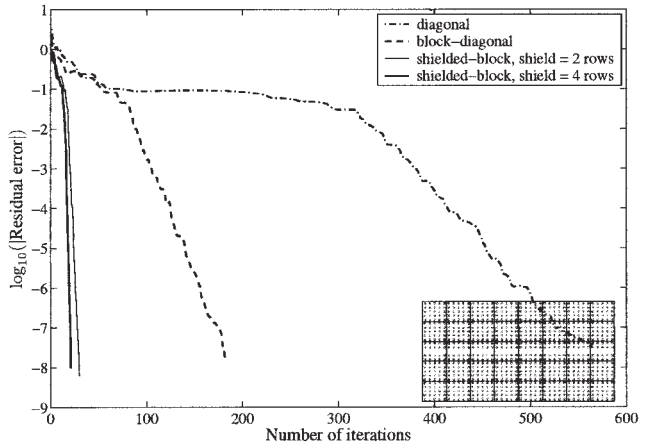

Figure 2 Residual error vs. iteration number for an EC waveguide

To better understand why the required number of iterations is higher for an EC waveguide than for a defectless EC, even when using a shielded-block preconditioner, the eigenvalues and corresponding eigenvectors of both the unpreconditioned and preconditioned interaction matrices $\boldsymbol{Z}$ and $\tilde{\boldsymbol{Z}}$ are calculated. Figure 3 shows the distribution of these eigenvalues in the complex plane for the defectless EC along with (the magnitude distribution of) some typical eigenvectors. The eigenvalues/vectors of $\boldsymbol{Z}$ basically come in two flavors: the eigenvectors corresponding to eigenvalues near the imaginary axis are concentrated primarily inside the EC while those corresponding to eigenvalues that track complex plane circles are concentrated near the EC edges. The exemplary performance of the shielded-block preconditioner when applied to the analysis of defectless ECs is due to the fact that it clusters all these eigenvalues around 1. In order not to overload the figures, the eigenvalues for the block-diagonal preconditioner are not shown here. Similarly to the shielded-block preconditioner, the block-diagonal preconditioner also clusters most of the eigenvalues around 1. However, contrary to the shielded-block preconditioner, it leaves some chaotically distributed eigenvalues. These eigenvalues are due to the interactions between edges of blocks, which are of course eliminated when including a shield. This explains the smaller iteration count for the shielded-block preconditioner. Figure 4 shows the distribution of the eigenvalues of the unpreconditioned interaction matrix describing an EC waveguide. The dis-

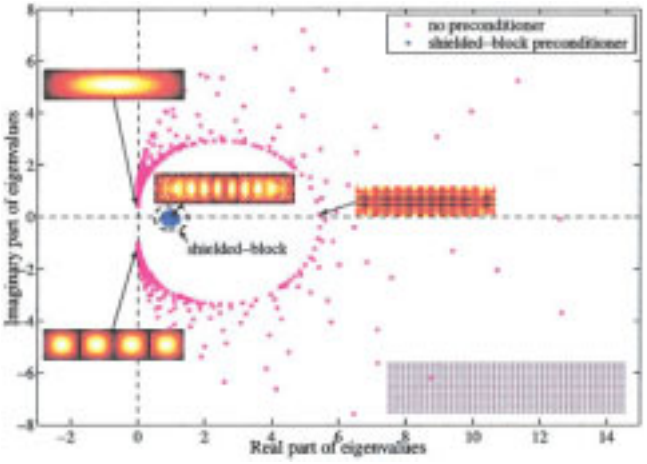

Figure 3 Distribution of the eigenvalues of the unpreconditioned and shielded-block preconditioned interaction matrix for a rectangular defectless EC (insets show some typical eigenvectors). [Color figure can be viewed in the online issue, which is available at www.interscience.wiley.com]

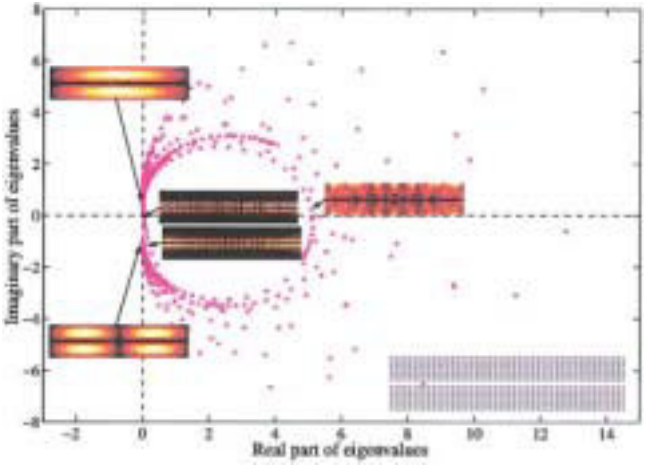

Figure 4 Distribution of the eigenvalues of the unpreconditioned interaction matrix for an EC waveguide (insets show some typical eigenvectors). [Color figure can be viewed in the online issue, which is available at www.interscience.wiley.com]

tribution of these eigenvalues and their typical eigenvectors are similar to those for the defectless EC, except that near the origin there is an extra line of eigenvalues with eigenvectors that are concentrated near the EC waveguide's channel. Figure 5 shows the distribution of the eigenvalues of the (shielded-block) preconditioned matrix $\tilde{\boldsymbol{Z}}$ for the same EC waveguide. Similarly to the defectless EC, all the eigenvectors with eigenvalues located inside or at the outer edges of the EC waveguide are clustered around 1. However, the abovementioned extra line of eigenvalues does not disappear, as the shielded-block preconditioner cannot resolve the guided mode interactions between all waveguide sections, thus explaining the higher iteration count.

3.3. Effect on Interaction Ranks and Matrix-Vector Multiplication Speed

This section details the effect of the shielded-block preconditioner on the numerical ranks of the submatrices of the preconditioned interaction matrix. Specifically, it shows that left-multiplication of the unpreconditioned interaction matrix $\boldsymbol{Z}$ with the shielded-block preconditioner automatically leads to a fast matrix-vector multiplication scheme. First note that, by its very definition, $\tilde{\boldsymbol{Z}} = \boldsymbol{I} + \tilde{\boldsymbol{Z}}^{\mathrm{nf}} + \tilde{\boldsymbol{Z}}^{\mathrm{ff}}$, where $\boldsymbol{I}$ stands for the identity matrix, $\tilde{\boldsymbol{Z}}^{\mathrm{nf}}$ comprises all near-field interactions between adjacent blocks, and $\tilde{\boldsymbol{Z}}^{\mathrm{ff}}$ comprises all far-field interactions between two nontouching blocks. Let $\tilde{\boldsymbol{Z}}^{\mathrm{ff}}_{ij}$ denote the submatrix of $\tilde{\boldsymbol{Z}}^{\mathrm{ff}}$ describing interactions between nontouching blocks i and j. Because ω lies within the EC bandgap, the rank of $\tilde{\boldsymbol{Z}}^{\mathrm{ff}}_{ij}$ typically is very low—this fact is elucidated below both on physical grounds as well as through computational experiments. This rank deficiency implies that the matrix-vector product $\tilde{\boldsymbol{Z}}^{\mathrm{ff}}\boldsymbol{A}$ can be evaluated quickly by approximating $\tilde{\boldsymbol{Z}}^{\mathrm{ff}}_{ij}$ by its truncated singular value decomposition, namely, by discarding all singular vectors with singular values below a set tolerance/noise floor:

$$\tilde{\boldsymbol{Z}}^{\mathrm{ff}}_{ij}\boldsymbol{A}_j \approx \tilde{\boldsymbol{U}}_{ij}\tilde{\boldsymbol{S}}_{ij}\tilde{\boldsymbol{V}}^{H}_{ij}\boldsymbol{A}_j. \tag{11}$$

Here, $\boldsymbol{A}_j$ denotes a vector comprising all unknowns of block j, $\tilde{\boldsymbol{S}}_{ij}$ is a $(R \times R)$ diagonal matrix containing the R largest singular values of $\tilde{\boldsymbol{Z}}^{\mathrm{ff}}_{ij}$, the matrices $\tilde{\boldsymbol{U}}_{ij}$ and $\tilde{\boldsymbol{V}}_{ij}$ contain $\tilde{\boldsymbol{Z}}^{\mathrm{ff}}_{ij}$'s left and right singular vectors, and $(\cdot)^H$ denotes the Hermitian conjugate. (In practice, rank-revealing submatrix decompositions other than the SVD are used, as they serve the same purpose while being cheaper to compute—see below.)

The rank deficiency of submatrices of $\tilde{\boldsymbol{Z}}^{\mathrm{ff}}$ can be traced to the bandgap character of the EC: for frequencies inside the electromagnetic bandgap, no fields can propagate through a defectless EC. As a result, upon preconditioning, blocks no longer interact through EC-immersed boundaries, but only through intended interaction ports or EC interfaces to the homogeneous background medium. This is illustrated by the three examples that follow. Figure 6 shows the evolution of the largest L singular values $\tilde{\boldsymbol{\sigma}}_{ij}(l)$, $l = 1, \ldots, L$, of $\tilde{\boldsymbol{Z}}^{\mathrm{ff}}_{ij}$, describing interactions between two densely filled blocks of cylinders embedded within a defectless EC as a function of shield thickness. All singular values decrease (exponentially fast) with increasing shield thickness, implying that, irrespective of the tolerance specified, the numerical rank of $\tilde{\boldsymbol{Z}}^{\mathrm{ff}}_{ij}$ becomes zero for a thick enough a shield. The insets in Figure 6 depict the corresponding singular vectors, proving again that the shield prevents electromagnetic fields from entering into the observer group. Figure 7 shows the same data when both blocks contain an EC waveguide. The evolution of the singular values is very similar to that in the previous example, except that the first

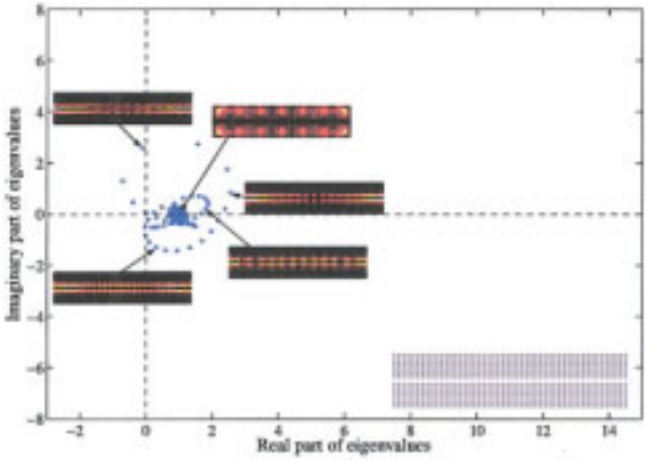

Figure 5 Distribution of the eigenvalues of the shielded-block preconditioned interaction matrix for an EC waveguide (insets show some typical eigenvectors). [Color figure can be viewed in the online issue, which is available at www.interscience.wiley.com]

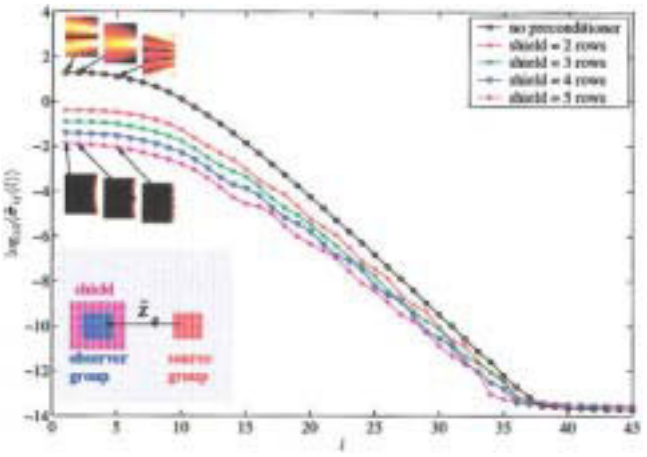

Figure 6 Evolution of the largest singular values of $\tilde{\boldsymbol{Z}}^{\mathrm{ff}}_{ij}$ as a function of shield thickness for two densely filled blocks that are completely immersed in the background EC. [Color figure can be viewed in the online issue, which is available at www.interscience.wiley.com]

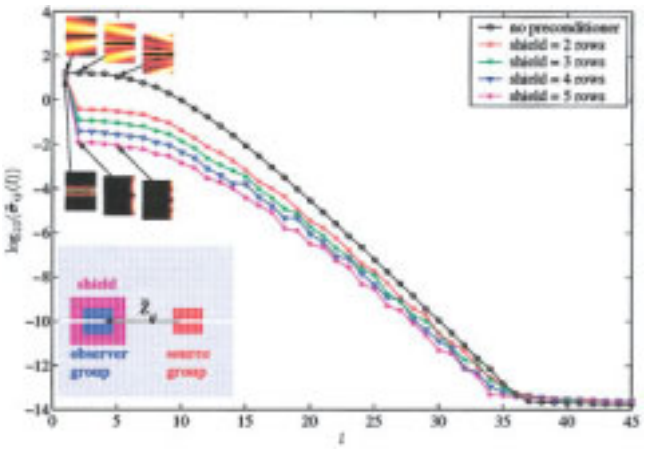

Figure 7 Evolution of the largest singular values of $\tilde{\boldsymbol{Z}}_{ij}^{\text{ff}}$ as a function of shield thickness for two blocks that contain an EC waveguide and are completely immersed in the background EC. [Color figure can be viewed in the online issue, which is available at www.interscience.wiley.com]

singular value stays put, irrespective of the shield thickness; this is due to the fact that in the example studied both waveguides support only a single propagating mode, which upon radiation from the shield aperture couples both blocks. Needless to say, the number of large singular values would increase for multimode waveguides. Figure 8 again shows the same data, but now for two densely filled blocks residing at the edge of a finite, defectless EC. As the observer block is only surrounded by a shield for three of its four edges, every singular value stays fixed from a certain thickness of the shield, demonstrating strong coupling between open facets (nearly) unaffected by shield thickness; the interaction rank, however, remains very low as long as the two exposed sides do not directly face one another (which rarely happens in real EC devices).

The above examples, while not exhaustive, are typical of most block interactions encountered when analyzing realistic EC devices. Obviously, the rank deficiency of $\tilde{\boldsymbol{Z}}_{ij}^{\text{ff}}$ greatly reduces the computational complexity of the matrix-vector product. The exact scaling law of the computational complexity heavily depends on the nature of the device studied and the shielding effectiveness of the actual bands of EC cylinders surrounding waveguides and cavities. While a detailed study of the computational complexity of the proposed scheme across different applications falls beyond the scope of this paper, our experience shows that for most practical devices the computational complexity of the matrix-vector product reduces to $O(N_c)$ for volumetric EC devices containing many inactive cylinders, and to $O(N_c^{1.5})$ for EC devices formed by cavities and waveguides lined by thin EC layers. These estimates assume that blocks contain $O(\sqrt{N_c})$ cylinders and that shields are thick enough to reduce interactions in the preconditioned system to those intended for proper device operation.

It is important to note that the bandgap character of the underlying EC can be exploited not only to accelerate the matrix-vector product, but also to cheaply construct all submatrices of the preconditioned interaction matrix. Indeed, if $\boldsymbol{Z}_{Ij}$ denotes the (unpreconditioned) interactions from the unknowns in block j to the unknowns in the larger block I, comprising block i and its shield, then $\tilde{\boldsymbol{Z}}_{ij} = \boldsymbol{Y}_i \boldsymbol{Z}_{Ij}$. As $\boldsymbol{Y}_i$ only contains the rows of $\hat{\boldsymbol{Z}}_i^{-1}$ pointing to unknowns in block i, the calculation of $\tilde{\boldsymbol{Z}}_{ij}$ requires that the unknowns are calculated on the cylinders of block i, when the cylinders in the larger block I are excited as dictated by the columns of Z_{Ij}. If the blocks i and j are nontouching, every column of Z_{Ij} corresponds to an excitation coming from outside block I. Due to the EC bandgap character and as demonstrated above, the number of independent solutions for the unknowns in block i is very low in this case. Hence, for these interactions, a low rank decomposition of $\boldsymbol{Y}_i$ can be obtained cheaply, for example, by using a rank-revealing QR decomposition or, preferably, a stochastic approach by randomly choosing a small set of linearly independent, orthonormalized plane waves and calculating the unknowns on the cylinders of block i due to each of these plane waves. If $\boldsymbol{U}_i$, $\boldsymbol{S}_i$, and $\boldsymbol{V}_i$ denote this decomposition of $\boldsymbol{Y}_i$, then $\tilde{\boldsymbol{Z}}_{ij} = \boldsymbol{U}_i \boldsymbol{S}_i \boldsymbol{V}_i^H \boldsymbol{Z}_{Ij}$. The last part $\boldsymbol{V}_i^H \boldsymbol{Z}_{Ij} = (\boldsymbol{Z}_{Ij}^H \boldsymbol{V}_i)^H$ can be evaluated cheaply using, for example, the fast-multipole method. Moreover, in most EC devices, the same block will be repeated frequently. If two blocks i and j are direct neighbors, $\boldsymbol{Y}_i$ can be decomposed using the new direct solvers recently developed by Martinsson et al. [17].

4. EXAMPLE: EC HORN ANTENNA ARRAY

Electromagnetic crystals have introduced new possibilities in the design of radiating structures, for example, ECs have been widely applied in the design of microwave antennas' substrates to reduce surface wave loss or to modify the radiation pattern. Recently, yet another application of ECs has been presented, namely, that of radiating horn-antenna arrays for optical beam steering [8, 9]. Optical beam steering is required in numerous applications, such as optical interconnection, communication, routing, and switching. An EC horn antenna is obtained from an EC defect waveguide by gradually tapering the waveguide's end to a larger opening, thereby forming the radiating aperture of the horn antenna. The advantages of such EC horn antennas in comparison with classical horn antennas are a large operating bandwidth, high directivity, low loss, and scalability.

Consider the EC horn antenna array depicted in Figure 9, comprising four basic EC horn antennas connected to a feed network of EC waveguides. The basic EC horn antenna presented in [8] was analyzed using the finite-difference time-domain method. Its taper length and taper angle are $21a$ and arctan(4/21), respectively. Note that near the inner edges of the horn antennas, cylinders are displaced from their regular place in the EC. The complete EC horn antenna array comprises 3600 cylinders, which corresponds to 10,800 unknowns ($K = 1$). The radiation pattern for $k_1 = 0.784(\pi/a)$ is given in Figure 10. For this example, the

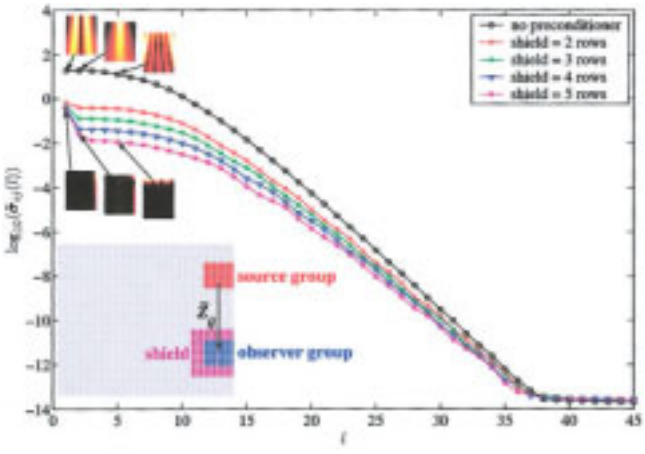

Figure 8 Evolution of the largest singular values of $\tilde{\boldsymbol{Z}}_{ij}^{\text{ff}}$ as a function of shield thickness for two densely filled blocks residing at the edge of a finite EC. [Color figure can be viewed in the online issue, which is available at www.interscience.wiley.com]

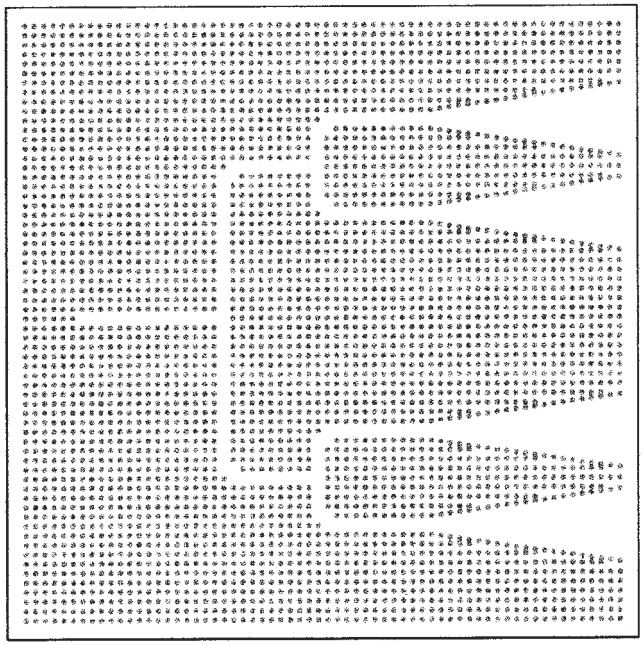

Figure 9 EC horn antenna array

blocks to form $\boldsymbol{M}$ are squares of 8×8 lattice constants. The shield thickness also is eight lattice constants. In this case, $\tilde{\boldsymbol{Z}}^{\mathrm{nf}}$ reduces to a zero matrix. Figure 11 shows the "rank map" of the (shielded-block) preconditioned interaction matrix for this EC horn antenna array when the noise floor below which all singular values are discarded is set to 10^{-6}. With this shielded-block preconditioner, the iterative solution of the system of equations given by (9) with transposed-free QMR to a tolerance of 10^{-5} requires only 17 iterations; using the proposed scheme, this takes 3.49 s on a dual AMD Opteron 244, 1.8-GHz PC. Using the multilevel fast multipole algorithm in combination with the same preconditioner, the iterative solution takes 29.2 s. Applying a block-diagonal preconditioner (with the same blocks), the iterative solution of the system of equations given by (9) requires 354 iterations, which takes more than 9 min using the multilevel fast-multipole algorithm. It is seen that the single-level preconditioner outperforms the multilevel fast-multipole algorithm. Moreover, recall that in the proposed scheme it is never necessary to explicitly compute the whole shielded-block preconditioner nor to store it, as every preconditioned submatrix can be calculated cheaply following the scheme given at the end of section 3.

5. CONCLUSION

A novel rank-revealing/shielded-block preconditioner for simulating wave propagation in 2D EC devices has been presented. First,

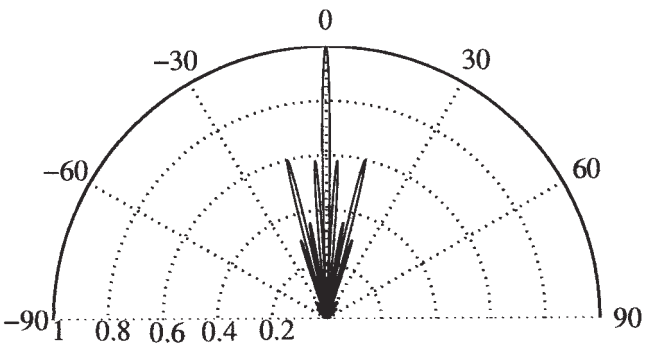

Figure 10 Radiation pattern of the EC horn antenna array

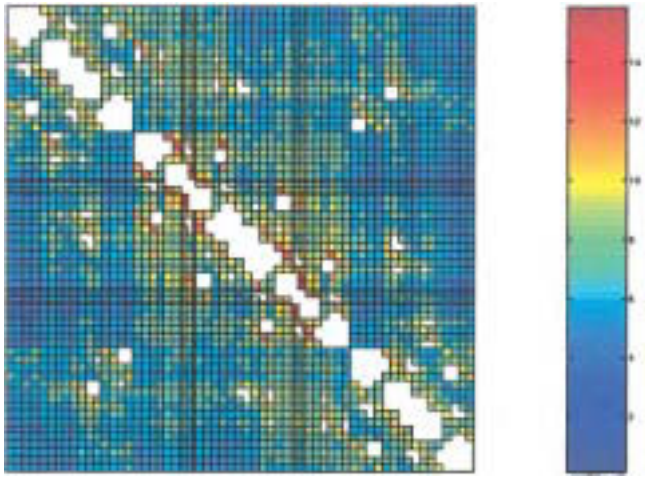

Figure 11 Rank map of the shielded-block preconditioned interaction matrix for the EC horn-array device (every small rectangle corresponds to a submatrix $\tilde{\boldsymbol{Z}}_{ij}^{\mathrm{ff}}$ and its color indicates the number of singular values larger than 10^{-6}. [Color figure can be viewed in the online issue, which is available at www.interscience.wiley.com]

it was demonstrated that the proposed preconditioner outperforms both diagonal and block-diagonal preconditioners in terms of the number of iterations required for convergence. Second, based on the bandgap character of an EC, it was shown that (i) premultiplication of the MST interaction matrix by the shielded-block preconditioner automatically leads to a fast matrix-vector multiplication scheme and (ii) the preconditioned interaction matrix can be calculated cheaply, with both following a rank-revealing decomposition. Even though this paper has focused on the application of the scheme to EC devices comprising circular scatterers arranged according to a square lattice and supporting TM_z-polarized fields, extensions of the proposed scheme to EC devices comprising noncircular scatterers and/or to other types of lattices and/or TE_z-polarized fields are trivial. In addition, multilevel extensions of the proposed preconditioner are being studied and will be reported elsewhere.

ACKNOWLEDGMENT

D. Pissoort acknowledges the Fund for Scientific Research, Flanders, Belgium (F. W. O.–Vlaanderen) for a postdoctoral fellowship.

REFERENCES

1. J.D. Joannopoulos, R.D. Meade, and J.N. Winn, Photonic crystals: Molding the flow of light, Princeton University Press, Princeton, NJ, 1995.
2. A. Mekis, J.C. Chen, I. Kurland, S. Fan, P.R. Villeneuve, and J.D. Joannopoulos, High transmission through sharp bends in photonic crystal waveguides, Phys Rev Lett 77 (1996), 3787–3790.
3. H. Benisty, C. Weisbuch, M. Agio, M. Kafesaki, C.M. Soukoulis, M. Qiu, M. Swillo, A. Karlsson, B. Jaskorzynska, A. Talneau, J. Moosburger, M. Kamp, A. Forchell, R. Ferrini, R. Houdré, and U. Oesterle, Models and measurements for the transmission of submicron-width waveguide bends defined in two-dimensional photonic crystals, IEEE J Quantum Electron 38 (2002), 770–785.
4. M. Koshiba, Wavelength division multiplexing and demultiplexing with photonic crystal waveguide couplers, J Lightwave Technol 19 (2001), 1970–1975.
5. S. Boscolo, M. Midrio, and C.G. Someda, Coupling and decoupling of electromagnetic waves in parallel 2D photonic crystal waveguides, IEEE J Quantum Electron 1 (2002), 47–53.
6. C. Jin, S. Han, X. Meng, B. Cheng, and D. Zhang, Demultiplexer using directly resonant tunneling between point defects and waveguides in a photonic crystal, J Appl Phys 91 (2002), 4771–4773.

7. L. Wu, M. Mazilu, T. Karle, and T.F. Krauss, Superprism phenomena in planar photonic crystals, IEEE J Quantum Electron 38 (2002), 915–918.
8. A.R. Weily, K.P. Esselle, and B.C. Sanders, Photonic crystal horn and array antennas, Phys Rev E 68 (2003).
9. C. Chen, S. Shi, D.W. Prather, and A. Sharkawy, Beam steering with photonic crystal horn radiators, Optical Engg 68 (2004), 174–180.
10. G. Tayeb and D. Maystre, Rigorous theoretical study of finite-size two-dimensional photonic crystals doped by microcavities, J Opt Soc Am A 14 (1997), 3323–3332.
11. D. Pissoort, D. De Zutter, and F. Olyslager, Efficient semi-analytical analysis of two-dimensional photonic crystals, IEEE AP-S Int Symp, Columbus, OH, Jun., 2003, vol. 3, pp 994–997.
12. W.C. Chew, J.M. Jin, E. Michielssen, and J. Song, Fast and efficient algorithms in computational electromagnetics, Artech House, Boston, 2001.
13. M.W. Beattie and L.T. Pileggi, Error bounds for capacitance extraction via window techniques, IEEE Trans CAD 18 (1999), 311–321.
14. D. Pissoort, E. Michielssen, F. Olyslager, and D. De Zutter, Fast analysis of 2D electromagnetic crystal structures using a periodic Green function approach, IEEE J Lightwave Technol 23 (2005), 2294–2308.
15. R.F. Harrington, Time harmonic electromagnetic fields, McGraw-Hill, New York, 1961.
16. R. Freund and N. Nachtigal, QMR: A quasi-minimal residual method for non-hermitian linear systems, Numer Math 60 (1991), 315–339.
17. P.G. Martinsson and V. Rokhlin, A fast direct solver for boundary integral equations in two dimensions, J Comput Phys 205 (2005), 1–23.

HIGHLY EFFICIENT LDMOS POWER AMPLIFIER BASED ON CLASS-E TOPOLOGY

Jongwoo Lee, Sungwoo Kim, Jungjin Nam, Jangheon Kim, Ildu Kim, and Bumman Kim
Department of Electrical Engineering
Pohang University of Science and Technology
San 31, Hyoja Dong, Nam Gu
Pohang, Gyeongbuk, 790-784, Republic of Korea

Received 15 October 2005

ABSTRACT: *This paper describes a highly efficient class-E power amplifier. The design has been carried out at 1 GHz using a LDMOS transistor with 10 W of peak envelope power (PEP). Drain efficiency of 76.1%, power-added efficiency (PAE) of 73.6%, and gain of 14.8 dB are achieved at an output power of 39.1 dBm for a continuous wave (CW) signal.* © 2006 Wiley Periodicals, Inc. Microwave Opt Technol Lett 48: 789–791, 2006; Published online in Wiley InterScience (www.interscience.wiley.com). DOI 10.1002/mop.21476

Key words: *class E; packaging effect; harmonic filtering; PEP; PAE*

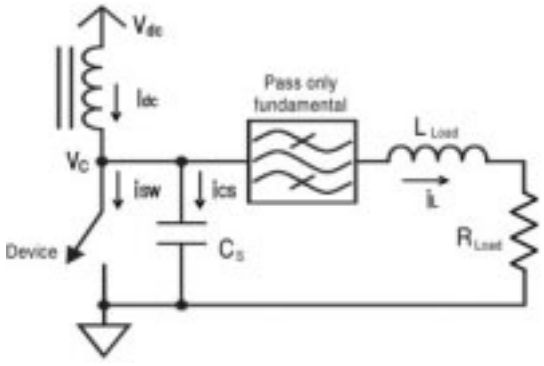

Figure 1 Configuration of basic class-E amplifier

TABLE 1 Class-E Design Parameters Using the Simplified Switch

R_{Load}	L_{Load}	C_S [pF]	C_{filter} [pF]
25.60	29.49	1.14	0.51
V_{DC_supply} [V]		P_{out_want} [V]	L_{filter} [nH]
21.07		10.00	50.00

1. INTRODUCTION

The efficiency of a power amplifier is directly connected with the thermal problem. As the efficiency becomes higher, the burden of heat sinking is lightened. And the volume and cost of the amplifier system can be reduced and the reliability of the system improved. High efficiency of an amplifier can be achieved by reducing the power dissipation of active devices and loss of an output network. The power dissipation in an active device can be minimized by eliminating the nonzero overlap of voltage and current waveforms. In a class-E amplifier, the transistor is operated as a switch to eliminate the overlap. The output network loss can be minimized by using a low-loss element such as a transmission line and employing a multisection matching for impedance transformation.

In this work, we have designed a highly efficient power amplifier based on the class-E topology using a commercially available LDMOS transistor. Parasitic elements of the device are compensated for proper class-E operation. For the implementation, the output network is implemented by transmission lines for the minimization of loss and suppression of harmonic power. Due to the structure optimization, we have achieved a state-of-the-art result from the class-E power amplifier.

2. DESIGN AND MEASUREMENT RESULTS

In the class-E amplifier shown in Figure 1, the active device is approximated by a switch [1]. If the switch does not have nonzero voltage and current simultaneously, the class-E amplifier does not dissipate any power in the active device. Such a condition can be satisfied by a proper selection of C_S, L_{Load}, and R_{Load} [2, 3]. Based on the operation concept, we have designed a class-E amplifier. The transistor used in this work is a Motorola MRF282 LDMOS, which is able to deliver an output power of 10 W with 40% efficiency and 11.5-dB gain at 2 GHz for a single tone. The operation voltage of device is 26 V and the minimum breakdown voltage is 65 V.

For the initial test, a simulation using a simplified switch with R_{on} of the transistor, which is 1.37Ω obtained from DC-IV of the device, has been carried out to extract the design param-

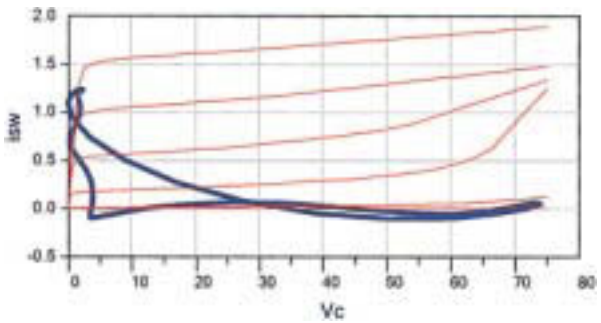

Figure 2 Simulated load-line of a class-E amplifier using the simplified switch. [Color figure can be viewed in the online issue, which is available at www.interscience.wiley.com]